DNA origami protection and molecular interfacing through engineered sequence-defined peptoids

Shih-Ting Wang[a], Melissa A. Gray[b], Sunting Xuan[c], Yiyang Lin[d,e,f], James Byrnes[g,h], Andy I. Nguyen[c], Nevena Todorova[i], Molly M. Stevens[d,e,f], Carolyn R. Bertozzi[b,j], Ronald N. Zuckermann[c], and Oleg Gang[a,k,l,1]

[a]Center for Functional Nanomaterials, Brookhaven National Laboratory, Upton, NY 11973; [b]Department of Chemistry, Stanford University, Stanford, CA 94305; [c]The Molecular Foundry, Lawrence Berkeley National Laboratory, Berkeley, CA 94720; [d]Department of Materials, Imperial College London, SW7 2AZ, London, UK; [e]Department of Bioengineering, Imperial College London, SW7 2AZ, London, UK; [f]Institute of Biomedical Engineering, Imperial College London, SW7 2AZ, London, UK; [g]Photon Science Division, National Synchrotron Light Source II, Brookhaven National Laboratory, Upton, NY 11973; [h]Energy Sciences Directorate, National Synchrotron Light Source II, Brookhaven National Laboratory, Upton, NY 11973; [i]School of Engineering, Royal Melbourne Institute of Technology, Melbourne, VIC 3001, Australia; [j]Howard Hughes Medical Institute, Stanford University, Stanford, CA 94305; [k]Department of Chemical Engineering, Columbia University, New York, NY 10027; and [l]Department of Applied Physics and Applied Mathematics, Columbia University, New York, NY 10027

DNA nanotechnology has established approaches for designing programmable and precisely controlled nanoscale architectures through specific Watson–Crick base-pairing, molecular plasticity, and intermolecular connectivity. In particular, superior control over DNA origami structures could be beneficial for biomedical applications, including biosensing, in vivo imaging, and drug and gene delivery. However, protecting DNA origami structures in complex biological fluids while preserving their structural characteristics remains a major challenge for enabling these applications. Here, we developed a class of structurally well-defined peptoids to protect DNA origamis in ionic and bioactive conditions and systematically explored the effects of peptoid architecture and sequence dependency on DNA origami stability. The applicability of this approach for drug delivery, bioimaging, and cell targeting was also demonstrated. A series of peptoids (PE1–9) with two types of architectures, termed as "brush" and "block," were built from positively charged monomers and neutral oligo-ethyleneoxy monomers, where certain designs were found to greatly enhance the stability of DNA origami. Through experimental and molecular dynamics studies, we demonstrated the role of sequence-dependent electrostatic interactions of peptoids with the DNA backbone. We showed that octahedral DNA origamis coated with peptoid (PE2) can be used as carriers for anticancer drug and protein, where the peptoid modulated the rate of drug release and prolonged protein stability against proteolytic hydrolysis. Finally, we synthesized two alkyne-modified peptoids (PE8 and PE9), conjugated with fluorophore and antibody, to make stable DNA origamis with imaging and cell-targeting capabilities. Our results demonstrate an approach toward functional and physiologically stable DNA origami for biomedical applications.

DNA nanotechnology | peptoid | molecular coating

DNA nanotechnology has advanced in programing the self-assembly of synthetic oligonucleotides into precisely prescribed molecular and nanoscale constructs with targeted topologies and spatial configurations (1–4). In applications, from electronics and photonics to biology and nanomedicine, DNA nanostructures with the appropriate attachment chemistries have been employed to direct controlled assembly of functional guest elements such as (bio)molecules and inorganic nanoparticles (NPs) (5–12). For biomedical functionalities, DNA origami has the potential to act as smart drug-delivery vehicles and biomolecular devices at the cellular level (13–17). In particular, DNA origami designed with controlled topology, biocompatibility, and responsiveness toward other biomolecules (e.g., proteins, liposomes, DNAs, and RNAs) provides a tailorable platform for engineering molecular interface and augmenting functionalities of the hybrid bio/nano system. For example, DNA-based logic-gated nanorobots for modulating cell signaling (18, 19) and DNA origami carriers loaded with small interfering RNA (20), CpG sequences

(21), enzymes (22, 23), and therapeutic drugs (24–26) were recently reported.

However, biomedical applications of DNA origamis are often incompatible with the high content of magnesium ions (10 to 20 mM) that are typically required for DNA origami self-assembly and long-term stability (27). Thus, the poor structural integrity of DNA origamis in physiological fluids, which typically contain ~1 mM Mg^{2+}, is one of the key challenges for establishing a therapeutic platform based on DNA origamis (28). Moreover, as the presence of enzymes (e.g., nucleases) and variation of solution pH can affect or even damage the DNA origami superstructures (28–30), it is crucial to seek new strategies to maintain their structural integrities and biological functions to facilitate broad biomedical applications.

Two major approaches have been investigated in previous studies to address these challenges. In the first approach, highly dense and stiff DNA origami structures, including the wireframed structures with polyhedral mesh (31, 32) and multiduplex DNA edges (33, 34), were explored to reduce unfolding and degradation of origamis caused by solution environments. Introduction of covalent cross-links to interlock the adjacent duplexes were also reported (29, 35, 36). For example, Gerling et al. (35) placed proximal thymidines

Significance

DNA nanotechnology provides a structural toolkit for the fabrication of programmable DNA nano-constructs; however, their use in biomedical applications is challenging due the limited structural integrity in complex biological fluids. Here, we report a class of tailorable molecular coatings, peptoids, which can efficiently stabilize three-dimensional wireframed DNA constructs under a variety of biomedically relevant conditions, including magnesium-ion depletion and presence of degrading nuclease. Furthermore, we show that peptoid-coated DNA constructs offer a controllable anticancer drug release and an ability to display functional biomolecules on the DNA surfaces. Our study demonstrates an approach for building multifunctional and environmentally robust DNA-based molecular structures for nanomedicine and biosensing.

to covalently link termini and cross-over sites or create new inter-helical connections via ultraviolet irradiation, allowing high thermal and ionic stabilities. Cassinelli et al. (36) applied click chemistry to catenate DNA strands, which enabled stable structures at low ionic strengths. The second approach involves noncovalent coating of DNA origamis with polyethylene glycol (PEG)-conjugated cationic polymers to stabilize against low Mg^{2+} contents in solution and to slow down nuclease degradation (37–39). Virus capsid proteins (40) and protein-cationic dendron conjugates (41) have also been used as coating layers to protect origamis against nucleases and enhance the transfection efficiency. In these approaches, electrostatic interactions between the positively charged moieties and the negatively charged DNA molecules are the key driving force for the adsorption of polycations onto DNA backbones. These localized polycations are thought to increase DNA stability by suppressing the interstrand repulsive force originating from the phosphate groups. Despite the progress in DNA origami protection strategies, it remains challenging to create molecularly precise and tunable protective coatings. This is critical in order to preserve origamis under a variety of biomedically relevant conditions that neither affect the structural integrity of origamis nor mask its shape and features. The objective of this study is to establish such a rational and tunable platform for designed molecular coatings of origamis that allow structural stabilization, chemical modularity, and biological versatility and to verify their efficacy in different biological environments.

In this work, we demonstrate that peptoid-based coating provides a tunable platform for protecting DNA nanostructures in a broad range of bioactive environments. Peptoids, comprising N-substituted glycines, are an emerging class of peptidomimetic molecules that offer biocompatibility, low-cost synthesis, high chemical flexibility, and designable sequences and performances (42–44). In a recent study, Xuan et al. (45) demonstrated that peptoid architectures could be engineered at the atomic level, resulting in a variety of atomically defined structural arrangements. Compared to peptides, peptoids possess high conformational flexibility and confer a high degree of resistance to proteolytic degradation (44, 46), due to the side chains located on the nitrogen of the amide backbone instead of the α-carbon. These tunable properties, as well as their intrinsic biocompatibility, offer

an attractive property for drug/gene delivery and cellular-imaging applications (47–50).

We focus this study on the investigation of a capability of peptoids with different architectures to protect DNA origamis in physiological conditions. The three-dimensional (3D) wireframed octahedra-shaped DNA origami (OC) was selected for this study for its mechanical stability, as well as the ability to carry nanoscale cargo. We exploit sequence-defined peptoids as structurally tunable polycations for the stabilization of OCs in bioactive solutions. The designed OC presents a rigid 3D structure that comprises six-duplex bundles at each edge (edge length ~ 29 nm) connected by the single-stranded M13mp18 DNA scaffold (Fig. 1B). This structure has been reconstructed from single-particle electron microscopy and applied to the creation of low-dimensional and 3D DNA–NP framework (51, 52). The frame design is also highly suitable for the immobilization of biomolecules and drugs of a range of sizes for biomedical applications due to the ability to design such structures with targeted sizes, affinities, and molecular-transport properties.

Here, we show that the design of peptoid sequences is key to mediating controlled peptoid–DNA interactions (schematic in Fig. 1C), the result of which leads to various protective effects in ionic and bioactive solutions and the ability to tailor DNA origami coatings. The developed strategy of peptoid coating is further explored in applications of the 3D DNA origami for drug release, proteolytic resistance, bioimaging, and targeted delivery. This work provides a platform for the stabilization of DNA origami structures based on peptoid–DNA interactions and provides molecular-level insights for expanding DNA origami use in drug/gene delivery and nanomedicine applications.

Results and Discussion

To protect DNA origami structures by surface coating with peptoids, we designed peptoid sequences with two types of monomers per chain, where one facilitated electrostatic complexation with the nucleic acids (i.e., positively charged motifs) and the other created surface passivation via hydrophilic PEG-like motifs. Furthermore, two types of polycationic peptoids were designed by varying the composition and spatial distribution to enable multivalent peptoid–DNA interactions and compact coating (Fig. 1A and *SI Appendix*, Fig. S1). In the brush-type peptoids (**PE1–3**), positively
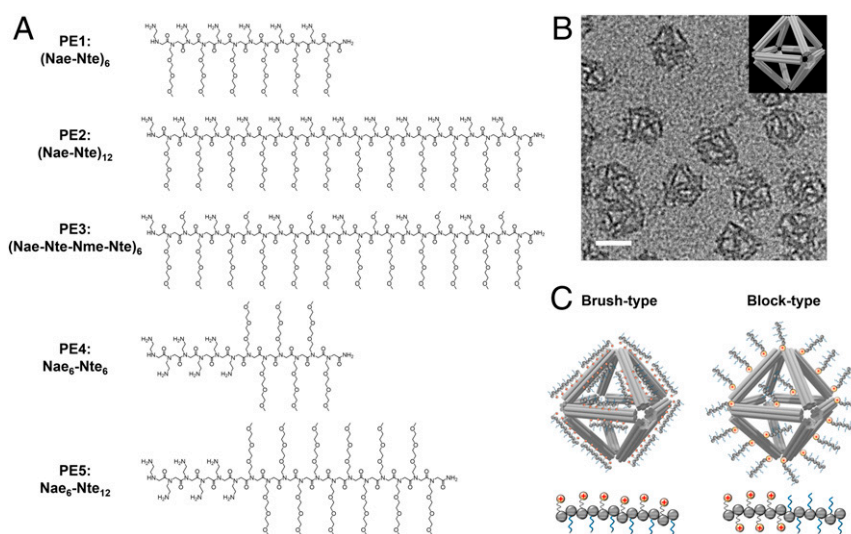

Fig. 1. Peptoids with different molecular architectures for DNA origami protection. (A) Chemical structures of peptoids designed to protect 3D OCs. PE1, PE2, and PE3 represent brush-type peptoids; PE4 and PE5 are block-type peptoids. (B) TEM image and schematic view (*Inset*) of the OC structure. (Scale bar, 50 nm.) (C) Schematic view showing the different surface coatings of the two types ("brush" and "block") of peptoids on OCs proposed in this work, which results in varied protection effects.

charged *N*-(2-aminoethyl)glycine (Nae) and neutral *N*-2-(2-(2-methoxyethoxy)ethoxy)ethylglycine (Nte) moieties were assembled alternately. In the block-type peptoids (**PE4–5**), Nae and Nte were clustered together to form "blocks" of the repeating units. These polycationic peptoids were designed to interact electrostatically to the anionic phosphate backbone of the DNA and compensate charge repulsions between DNA strands. As a control experiment, brush-type (**PE6**) and block-type (**PE7**) peptoids with Nae substituted by similarly sized, but neutral, monomer *N*-(2-methoxyethyl)glycine (Nme) were studied. Meanwhile, a highly solvated and unstructured domain by the incorporation of neutral Nte oligomers was designed to preserve DNA origami structures during the peptoid–DNA electrostatic interactions. The ether side chain, like in the Nte monomers, has been shown in previous peptoid studies to exhibit antifouling and surface passivation properties. That can prevent surface adsorption of biomolecules in physiological environments and inhibit enzymatic degradation of DNA origamis due to proteases and nucleases (44, 46, 53, 54).

In this paper, the binding between a single-duplex DNA and peptoids was first studied by experimental methods and molecular dynamics (MD) simulations to elucidate the effect of peptoids of different designs on a duplex. The observed influence of peptoid architecture and sequence on the enhanced stability of single duplexes were further exploited to stabilize 3D OCs in physiological solutions. This includes the depletion of magnesium ions (Mg^{2+}), the presence of nuclease, and the addition of cell-culture media. The functionality of peptoid-stabilized OCs was also explored, where controlled release of an anticancer drug and tryptic digestion of proteins encapsulated in OC nanostructures were studied. Finally, alkyne-modified peptoids (**PE8** and **PE9**) were used to conjugate functional biomolecules and present them on the surface of peptoid-stabilized OCs.

The effect of the two types (i.e., brush and block) of peptoid architectures on stabilizing a single-duplex DNA (double-stranded DNA [dsDNA]) was investigated by real-time SYBR Green I (SG) fluorescence assay. SG is known to have a stronger affinity toward dsDNA than to single-stranded DNA (ssDNA) due to the favored intercalation between base pairs and the increased stability of the SG/dsDNA complex (55, 56). The fluorescence assay is based on the enhanced SG fluorescence in complex with dsDNA, which originates from the dampening of its intramolecular motion (55, 56). Here, a 15-base-pair dsDNA with a melting temperature (T_m) of ~44 °C was designed to study dsDNA stability in the presence of peptoids at varied molar ratios of peptoid amines to phosphate groups of the DNA (i.e., N/P). In the experimental setup, the temperature was raised from 37 °C to 85 °C and equilibrated at every 1 °C step for 5 min. At all measured temperatures (≥40 °C), fluorescence signals of SG/dsDNA complexes were observed to be higher in the presence of peptoids, indicating an enhanced stability of DNA base-pairing (Fig. 2*A* and *SI Appendix*, Fig. S2). The increase of fluorescence signal can be related to the association of SG with dsDNA (55), since no signal was observed when SG was mixed with peptoids only (*SI Appendix*, Fig. S3). T_m of dsDNA/peptoid complexes was presented by the derivative of fluorescence intensities and plotted against temperature. As shown in Fig. 2 *B* and *D* and *SI Appendix*, Fig. S2, depending on the amount of peptoid added, T_m of the dsDNA increased modestly from 1 °C to 6 °C. Among the sequences, **PE2** exhibited the highest performance in raising T_m of the dsDNA, where the T_m shifted from 44 °C to 50 °C as the N/P increased from 0.125 to 8 (Fig. 2 *C* and *D*). Moreover, brush-type peptoids were observed to confer higher stability of the dsDNA compared to block-type peptoids, where T_m (dsDNA/PE2) > T_m (dsDNA/PE1) > T_m (dsDNA/PE4) and T_m (dsDNA/PE3) > T_m (dsDNA/PE5) (Fig. 2 *A* and *B*).

In the previous study, it was shown that polycationic polymers and lipids often cause DNA to form polyplexes due to charge neutralization. Such aggregated structures can significantly quench
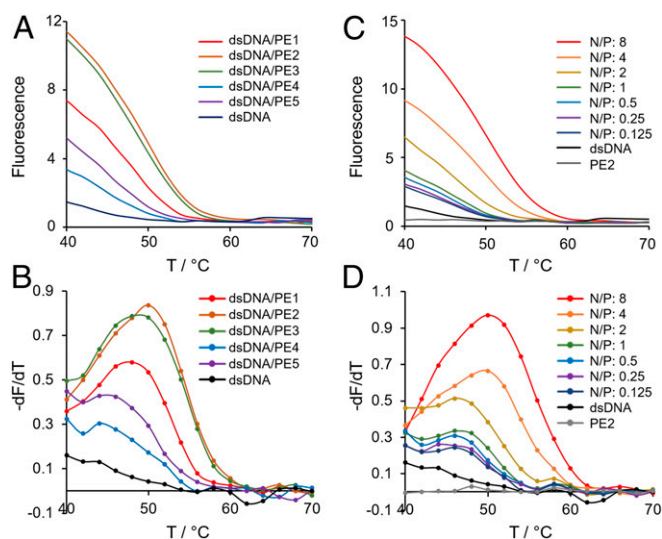

Fig. 2. Fluorescence assay monitoring peptoid-stabilized duplex DNA (dsDNA). Real-time SG fluorescence assay of a 15-bp dsDNA (500 µM) in the presence of peptoids at different ratios of peptoid amines to phosphate groups of the DNA (N/P) is shown. The fluorescence intensities of dsDNA/peptoid complexes at N/P of 4 (*A* and *B*) and dsDNA/PE2 complexes at different N/P (*C* and *D*) are plotted against the increasing temperature. In *B* and *D*, derivatives of fluorescence intensities representing the melting temperature (T_m) of dsDNA are plotted against the increasing temperature.

DNA-binding fluorophores (57). Here, the hydrophilic Nte oligomers in the peptoid sequences were designed to inhibit DNA condensation and polyplex formation. We investigated the effect using **PE2**, which succeeded in raising the T_m of dsDNA among the studied peptoids. Indeed, the fluorescence of SG intercalated inside the dsDNA remained unchanged after the addition of **PE2** at room temperature (25 °C) (*SI Appendix*, Fig. S4). This was confirmed by agarose gel electrophoresis (AGE), where no aggregation of dsDNA/PE2 was noted at N/P from 0.125 to 8 (*SI Appendix*, Fig. S5). These indicated that the peptoid–dsDNA interactions did not induce DNA condensation at the studied N/P regimes.

Explicit solvent MD simulations were performed to reveal the binding mechanisms of peptoids of brush and block architectures with dsDNA in solution (Fig. 3 *A* and *B* and *SI Appendix*, Fig. S6 and Table S1). Following the experimental findings from the fluorescence assay (Fig. 2*A*), we selected the distinct brush-type **PE1** and block-type **PE4** as representative peptoid models to study the peptoid–dsDNA interactions at N/P of 0.25 using MD simulations. The simulations were performed at corresponding experimental conditions in neutral pH (*Materials and Methods*). As shown in *SI Appendix*, Table S1, the simulations showed strong binding affinities of both types of peptoids to dsDNA, of which **PE1** and **PE4** exhibited persistent contacts (cutoff = 4 Å) for 98.2% and 98.7% of the total simulation time, respectively. The peptoids experienced almost immediate binding to the dsDNA, regardless of their starting structures in the simulations. This strong attraction was due to the electrostatic attractive forces between the positively charged Nae residues of the peptoids and negatively charged phosphate groups of the DNA backbone.

Despite the comparable strong binding, **PE1** and **PE4** exhibited distinct differences in the binding mechanisms to dsDNA. Brush-type **PE1** demonstrated persistent interactions (~98% of the total contact time) with DNA via both the Nae and Nte motifs, where at least 58% (Nae) and 61% (Nte) of the time, three or more residues were in close contact with the dsDNA. In addition, the "brush" arrangement facilitated **PE1** to spread across ("coat") the DNA backbone, where it interacted with both major and minor
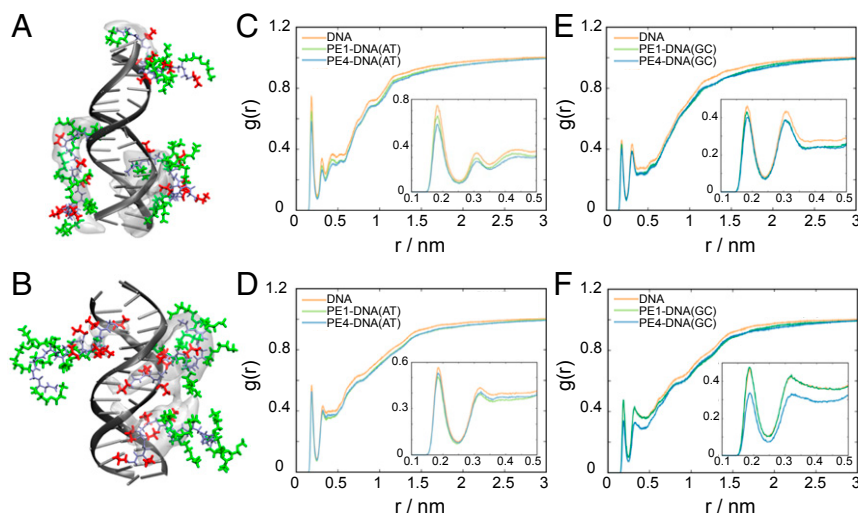
Fig. 3. MD simulations of the interactions of PE1 and PE4 with dsDNA. (*A* and *B*) Molecular representation of the most visited binding sites and structures of PE1 (*A*) and PE4 (*B*) with dsDNA (blue, peptoid backbone; orange, Nae residues; green, Nte residues). The most visited binding sites are represented as occupancy volume areas (shown as transparent white), where the peptoids are present for at least 6% of total contact time. (*C–F*) RDFs of water near the minor (*C* and *D*) and major (*E* and *F*) grooves of the dsDNA. RDFs were calculated on the H (donor) atoms of water and the N and O (acceptor) atoms of AT (*C* and *E*) and GC (*D* and *F*) base pairs. The structuring of water around pristine DNA is shown in orange, and the dsDNA/PE1 and dsDNA/PE4 complexes are shown in green and blue, where the AT and GC base pairs are distinguished by light and dark colors, respectively. The *Insets* show a magnified representation of the first two peaks of the RDF results.

grooves concurrently (48.8% of the total contact time). Preferred binding toward the minor groove (28.5%) exclusively over the major groove (6.1%) of the dsDNA was also observed.

In contrast, the block-type peptoid **PE4** dominated binding to dsDNA via the Nae moieties (∼100% of the total contact time), where four or more Nae residues were in close contact with the dsDNA for more than 85% of the time. Meanwhile, the Nte moieties exhibited significantly less persistent interactions with DNA, where only the closest two Nte residues were involved in binding for 55% of the total contact time. In addition, the "block-like" arrangement facilitated the Nte end of **PE4** to be solvent exposed, and, therefore, **PE4** was observed to embed in either the major (39.6%) or minor (24%) grooves of the dsDNA, while simultaneous interactions with both major and minor grooves (18.5%) were less favored. As expected, **PE1** formed a larger contact area with dsDNA (2.88 ± 1.11 nm^2) compared to **PE4** (2.54 ± 1.05 nm^2). However, the average solvent-accessible surface area of **PE4** (17.81 ± 1.64 nm^2) was lower than that of **PE1** (18.82 ± 1.47 nm^2), due to the more compact structure adopted by **PE4** compared to the elongated **PE1** while being bound to DNA (*SI Appendix*, Table S1). Interestingly, the MD simulations showed the **PE1** structure to be more flexible and dynamic while interacting with the dsDNA compared to **PE4**, which was frequently restrained due to the embedding of the Nae moieties within the DNA grooves (demonstrated by the larger occupancy volume areas adopted by **PE4** compared to **PE1** in Fig. 3 *A* and *B*).

We propose that water plays an important role in the binding phenomena of the different peptoid architectures with dsDNA. The structural organization of water surrounding the pristine dsDNA and the dsDNA/peptoid complex was investigated by radial distribution functions (RDFs). Fig. 3 *C–F* show a higher density of water molecules surrounding AT base pairs versus GC base pairs, with notable preference for the AT base pairs within the minor grooves. The higher solvation of the minor groove, vis-à-vis the major groove of DNA, was reported (58). Interestingly, the binding of **PE4** contributed to significant expulsion of water from the dsDNA, with the most evident reduction in water density at the minor grooves of the AT base pairs and major

grooves of the GC base pairs. We propose that this was due to the block-like arrangement of **PE4**, where the "block," comprising osmotic ethylene glycol residues could alter the surrounding dielectric constant, resulting in effective displacement of water molecules from the DNA structure (59, 60). On the other hand, **PE1** was observed to have the least effect on the structuring of water surrounding the dsDNA, suggesting that such a "brush-like" arrangement of **PE1** did not impact the water uptake by dsDNA. Thus, we propose that water can facilitate the interactions of the polar Nte moieties to achieve a close (albeit dynamic) binding and larger contact area with the dsDNA. Since it is known that DNA hydration is directly related to the stability of duplex formation, specifically through Watson–Crick base pairs (61), the observed differences in water structuring and binding mechanisms of **PE1** and **PE4** to dsDNA play important roles in the stability of dsDNA. Thus, the simulations are in a close correspondence with the results obtained from the SG fluorescence assays (Fig. 2), and such observations can be extended to elucidate how peptoids bind to DNA.

Guided by the experimental and simulation studies on the effect of peptoid design toward interactions with DNA, we investigated the structural stability of OCs coated by peptoids. As shown in *SI Appendix*, Fig. S7, transmission electron microscopic (TEM) imaging showed that the morphology of OCs was maintained when N/P was below 0.5. Higher N/P could lead to an aggregated structure. This was improved by increasing the number of Nte residues, of which **PE2** ((Nae–Nte)$_{12}$) and **PE3** ((Nae–Nte–Nme–Nte)$_6$) OCs exhibited higher structural integrity than **PE1** ((Nae–Nte)$_6$). Similarly, increasing the number of Nte residues in the block-type peptoids, **PE4** (Nae$_6$–Nte$_6$) and **PE5** (Nae$_6$–Nte$_{12}$), to 16 Nte residues enabled more stable OC structures (*SI Appendix*, Figs. S7 and S8). This suggests that incorporation of the hydrophilic Nte motifs promotes a stabilization of DNA origami during polycation–DNA charge neutralization. It is noteworthy that the OC structure is composed of ∼120 dsDNA fragments, and, thus, not only does the peptoid coating (i.e., **PE2**) stabilize the origami structure by maintaining its 3D configuration, but it may facilitate a base-paring of individual dsDNA fragments (Fig. 2). An SG assay was performed

on OC/peptoid (N/P: 0.125) to confirm this effect, where OC/PE2 exhibited a clear T_m shift from 48 °C to 52 °C (*SI Appendix*, Fig. S9).

On the other hand, **PE6** and **PE7** peptoids, where the positively charged Nae residues were substituted by neutral Nme residues on the peptoid backbone, exhibited no obvious structural changes at even higher N/P (i.e., 0.5, 1, and 2; *SI Appendix*, Figs. S10 and S11). This supports that the Nae moieties are the primary driving force for the peptoid–DNA interactions as demonstrated by the MD simulations (Fig. 3). The ζ potential was also analyzed ($n = 3$), where bare OCs and **PE2**- and **PE3**-coated OCs were measured at −13.3 ± 0.34, −11.7 ± 0.42, and −12.6 ± 0.40 mV, respectively. The low ζ potential of OCs was

likely due to the high ionic strength and Mg^{2+} content of the buffer, which effectively shielded the surface charge of OCs.

Mg^{2+} is known to play a central role for the integrity of DNA origami nanostructures by stabilizing DNA base-pairing and reducing interduplex repulsion (28). Here, an Mg^{2+}-depleted condition was generated by diluting the bare OCs and peptoid-coated OCs (OC/peptoid) so that the final concentration of magnesium chloride ($MgCl_2$) in solution was 1.25 mM (schematic in Fig. 4A). The structural integrity of OCs was first assessed by AGE. The peptoid-protected OCs showed bands on the agarose gel similar to bare OCs, confirming the intact OC nanostructures (*SI Appendix*, Fig. S12). However, when $MgCl_2$ concentration was reduced from 12.5 to 1.25 mM, a notable electrophoretic band shift in the agarose gel was observed (Fig. 4 *B* and *C* and *SI Appendix*,
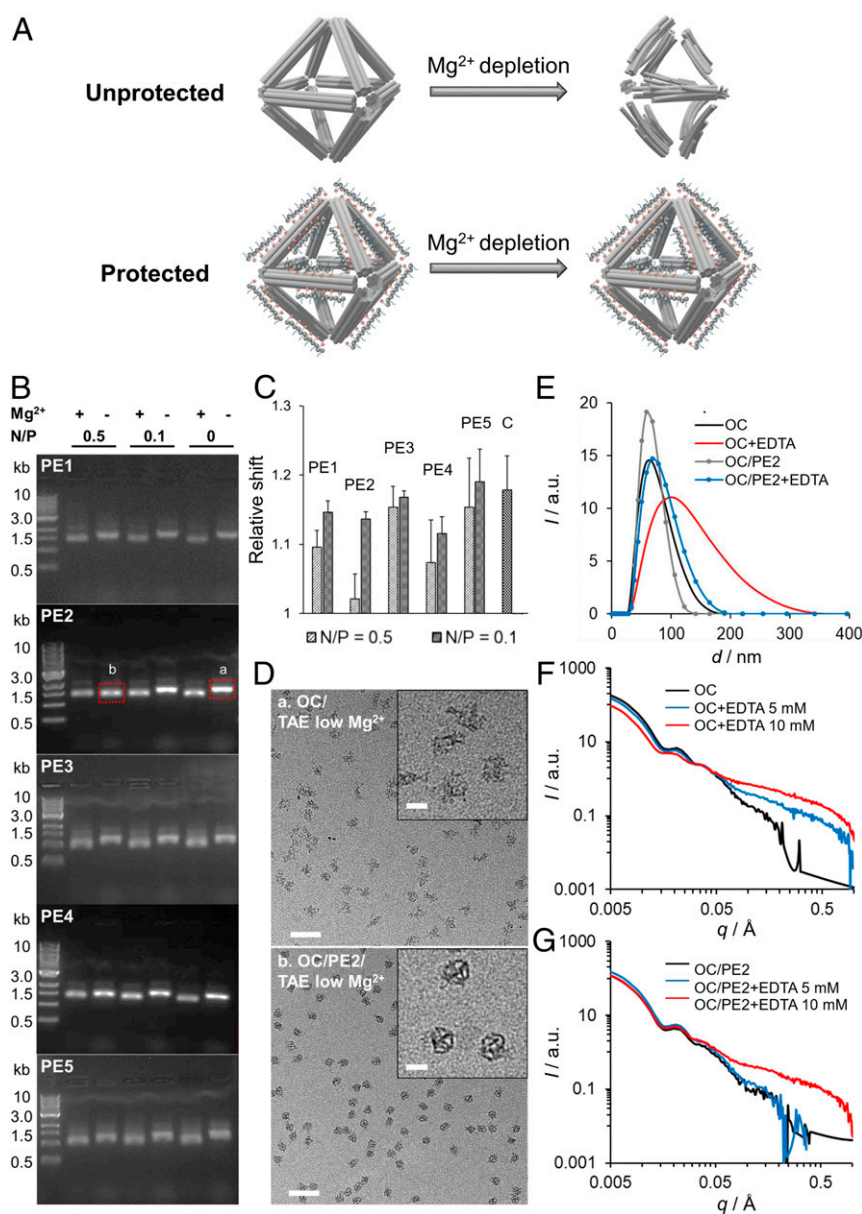

Fig. 4. Analysis of peptoid-coated OCs in low-Mg^{2+} solution. (*A*) Schematic view showing peptoid-coated OCs (OC/peptoid) protection against Mg^{2+} depletion. (*B* and *C*) AGE was used to analyze the structural integrity of OCs in TAE buffer at $MgCl_2$ concentrations of 12.5 mM (+) and 1.25 mM (−). In *C*, the electrophoretic shift was measured from the reference band at 0.5 kb and the relative value was calculated from that of the control OCs ($n = 3$). (*D*) TEM imaging was performed on OCs extracted from the agarose gels (bands a and b in *B*). (Scale bars, 200 nm.) *D*, *Insets* show magnified images of the OC structures. (Scale bars, 100 nm.) (*E* and *F*) DLS (*E*) and in situ SAXS (*F*) spectra for bare OC and OC/PE2 systems treated with EDTA (5 or 10 mM) for 20 to 30 min at room temperature. a.u., arbitrary units.

Fig. S13), indicating the damage of OCs at this ionic condition. At N/P of 0.5, OC/peptoid showed less electrophoretic shift than bare OCs, indicating an improved stability in the presence of peptoids (Fig. 4C). Among the peptoid sequences, OC/PE2 showed the least electrophoretic shift at N/P of 0.5, while the protection effect was significantly reduced at N/P of 0.1, supporting that higher concentration of positively charged moieties could compensate the depletion of Mg^{2+}. TEM imaging was further performed on bare OCs, and OC/peptoid structures were extracted from the agarose gel. As shown in Fig. 4D and *SI Appendix*, Fig. S14A, the structure of bare OCs in a low-Mg^{2+} condition was significantly distorted and expanded. At an N/P of 0.5, TEM imaging indicated that a dense coating of **PE2** did not compromise the structural integrity of OCs in the Mg^{2+}-depleted solution (Fig. 4D and *SI Appendix*, Fig. S14), while the protection effect was not observed for other peptoid sequences (*SI Appendix*, Fig. S15). This stronger PE2–DNA interaction was consistent with results obtained from the SG assays (Fig. 2).

To probe in-solution structures of the peptoid-coated OCs, we applied dynamic light scattering (DLS) and in situ small-angle X-ray scattering (SAXS), which provide an average size of bare OC and OC/PE2 structures and information about their internal organization. Here, ethylenediaminetetraacetic acid (EDTA), a strong metal-ion chelating reagent, was used to remove Mg^{2+} from the solution, where TEM images showed that the extent of damaged OCs increased with the increasing concentration of EDTA (*SI Appendix*, Fig. S16). As shown in Fig. 4E, DLS revealed a broadening of a size distribution when the bare OCs were treated with a high concentration of EDTA (10 mM), indicating a loss of structural integrity of the OCs and increased heterogeneity of the OC population. On the other hand, peak broadening was effectively inhibited by **PE2** coating, suggesting that OC stability was significantly improved in the presence of **PE2**. Similarly, SAXS showed that the q value at 0.021 $Å^{-1}$, representing the form factor of OCs, continued to shift toward the lower q regime in the presence of EDTA (5 and 10 mM) for bare OCs, which indicates an overall size increase due to OC disintegration. In contrast, the structural changes of OCs were effectively inhibited by **PE2** coating (Fig. 4 F and G), with only some destabilization observed at higher EDTA concentrations. We note the differences in the scattering profiles at large q for moderate (5 mM) and high (10 mM) EDTA for bare and OC/PE2, respectively, indicating that the origin of destabilization was on the scale of DNA bundles and duplexes. Once the duplexes were disrupted, the nanoscale structure of origami and its overall shape might degrade. The flexibility, or "unfoldedness," of the
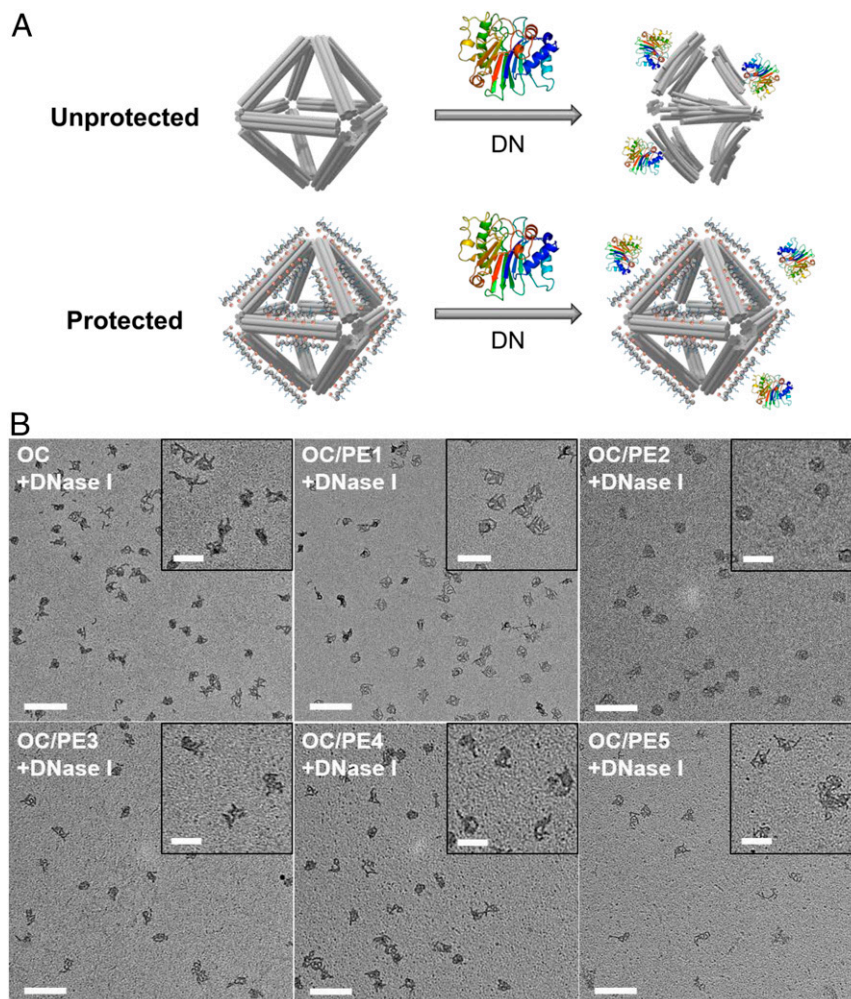

Fig. 5. Structural analysis of peptoid-coated OCs in the presence of DNase. (A) Schematic view showing peptoid-coated OCs (OC/peptoid) protected against DNase I degradation. Adapted with permission from PDB ID: 2DNJ (68). (B) TEM images show bare OC and OC/peptoid structures (N/P: 0.5) in solution containing DNase I concentration of 15 μg/mL TEM imaging was performed on samples extracted from the agarose gel. (Scale bars, 200 nm.) B, Insets show magnified images of the OC structures. (Scale bars, 100 nm.)

OC structures obtained from SAXS were also assessed by using the Kratky analysis (62). As shown in *SI Appendix*, Fig. S17, bare OCs became more flexible and did not plateau at higher q upon treatment with EDTA, while this effect was inhibited by **PE2** coating. These results were consistent with AGE and TEM imaging (Fig. 4 *B–D* and *SI Appendix*, Fig. S14).

When bare OC and OC/peptoid systems were dispersed in phosphate-buffered saline (PBS) at low Mg^{2+} content, all OC/peptoid exhibited more stable structures compared to those observed in Tris–acetate–EDTA (TAE) buffer (*SI Appendix*, Fig. S18). This was likely due to the Na$^+$ in PBS buffer compensating the loss of Mg^{2+} and assisting the stability of OC structures.

To study the ability of OC/peptoid to resist enzymatic degradation, we investigated the OC/peptoid in solution containing deoxyribonuclease I (DNase I) (schematic in Fig. 5*A*). As shown in AGE, bare OCs could be degraded by DNase I at a concentration as low as 2.5 µg/mL, where the increased electrophoretic mobility suggested a dissociation of staple strands from the OCs (*SI Appendix*, Fig. S19). To demonstrate the protecting effect of peptoids, bare OCs and OC/peptoid were incubated with DNase I (15 µg/mL) for 30 min at 37 °C and inspected by TEM imaging (Fig. 5 and *SI Appendix*, Fig. S20). As expected, bare OC structures were degraded, and the octahedra shape was damaged after incubating with DNase I. In the presence of peptoids, the OC/PE2 structure remained intact, and **PE1**, **PE3**, and **PE4** showed the ability to preserve the OC structure. DLS also confirmed a smaller size reduction of the OC/PE2 at DNase I levels of 15 and 20 µg/mL compared to bare OCs (*SI Appendix*, Fig. S21). We propose that the stronger multivalent interactions in the OC/PE2 system provides a tighter binding of **PE2** and that hinders DNase I adsorption to both dsDNA and ssDNA motifs, which significantly reduces the degradation effect of DNase I. The Nte oligomers of the peptoid sequences are also likely to provide steric shielding to reduce DNase I binding to the DNA backbone. To suppress the enzymatic degradation of DNA nanostructures, the peptoid-coating approach discussed here can potentially be combined with the denser design of DNA origami objects, staple routing, and a minimal number of ssDNA fragments (33, 34). At the same time, due to the diversity of nuclease processes (63), the presented strategy of molecular coating might be beneficial for the protection of DNA origami of various designs.

To explore the peptoid-promoted stability of OCs in cell media, we used **PE2** since it has exhibited the best protection in the experiments discussed above. We investigated OC/PE2 in Dulbecco's modified Eagle medium (DMEM) (Fig. 6 *C* and *D* and *SI Appendix*, Fig. S22) and Roswell Park Memorial Institute (RPMI) 1640 medium (Fig. 6 *A* and *B*) in a low-Mg^{2+} condition. TEM images showed that OC/PE2 (N/P: 0.5) were protected after incubating in both the RPMI and DMEM media at 37 °C for 24 h, while the OC structures were distorted without **PE2** coating (Fig. 6 and *SI Appendix*, Fig. S22). In the presence of fetal bovine serum (FBS), the combination of Mg^{2+} depletion and FBS nuclease led to enhanced structural damages of bare OCs beyond recognition (Fig. 6*C*). On the other hand, TEM imaging showed the presence of stable OC/PE2 in the DMEM–FBS medium, although the reduced number of OCs was observed after incubation at 37 °C for 24 h (Fig. 6*D*). The protection is expected to be further improved by increasing the length of the **PE2** sequence, enabling stronger peptoid–DNA interactions while preventing OC aggregation; that requires further experimentation. In an independent experiment, 10-nm gold (Au) NPs were encapsulated in the OC structures by surface functionalization of Au NPs with ssDNAs that complemented eight ssDNA linkers located in the OCs prior to **PE2** coating (*SI Appendix*, Fig. S23). As shown in *SI Appendix*, Fig. S24, the Au NPs remained encapsulated in the OC/PE2 after incubation in the DMEM and DMEM–FBS media at 37 °C for 24 h. This observation further demonstrates that **PE2** coating can even provide protection for nano-cargo that is hybridized inside 3D origami.

The resistance of OC/PE2 against Mg^{2+} depletion, change in buffer component, and nuclease degradation make it an attractive candidate for biomedical applications of DNA origami. To this end, we explored the capability of OCs in drug and protein immobilization and studied their peptoid-enhanced stabilities for potential applications. We loaded doxorubicin (Dox), a common anticancer drug used in chemotherapy, to bare OCs and OC/PE2 (N/P: 0.5) and measured its release from the OC structures. Dox-loaded DNA origamis have been reported in the literature, where the molecule intercalates the DNA backbone and releases from the origami structures over time (24–26), but methods to control its release in time were not established. The intrinsic Dox fluorescence could be used to measure the loading and release from the OCs (24–26), where the fluorescence intensity is proportional to the Dox concentration in the submicromolar range (*SI Appendix*, Fig. S25). In our case, ~10% of Dox was loaded onto the OCs. As shown in *SI Appendix*, Fig. S26, a reduction of the total Dox release from the OC/PE2 (~10% release) compared to bare OCs (~30% release) was observed at both pH 7 and 5.5 after incubating at 37 °C for 48 h in PBS buffer. Such
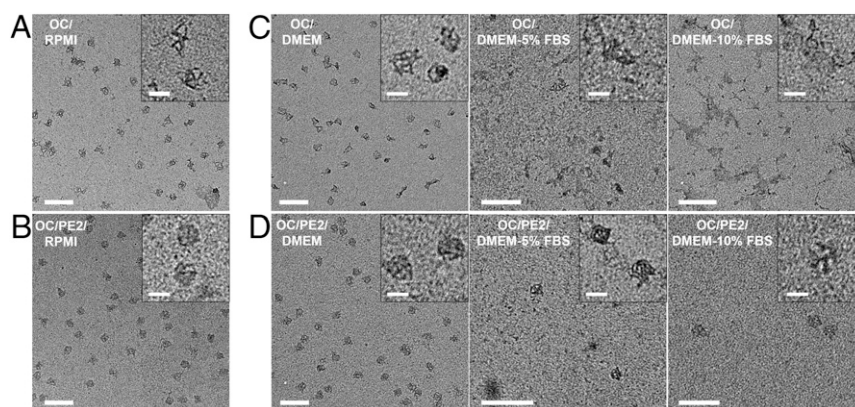

Fig. 6. The effect of peptoid coating of OCs in cell media and presence of serum nuclease. TEM images show bare OCs (*A* and *C*) and PE2-coated OCs (OC/PE2) (*B* and *D*) in RPMI (*A* and *B*) and DMEM (*C* and *D*) containing 0%, 5%, and 10% FBS and incubated at 37 °C for 24 h. The final concentrations of MgCl$_2$ were 1.25 mM. TEM imaging was performed on samples extracted from the agarose gels. (Scale bars, 200 nm.) *A–D, Insets* show magnified images of the OC structures. (Scale bars, 50 nm.)
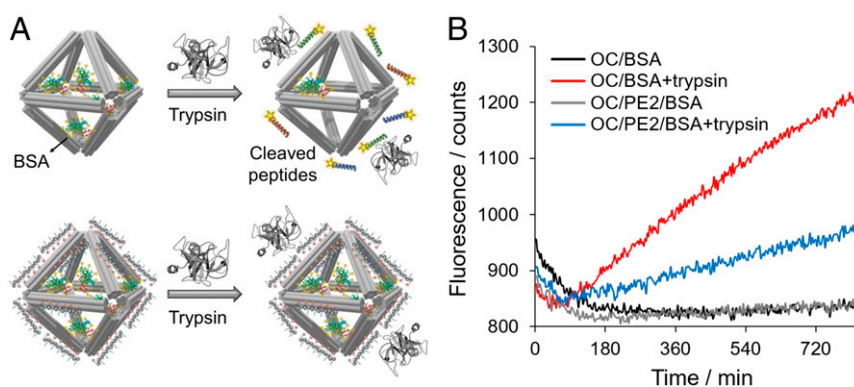
Fig. 7. Protection of protein-encapsulated in OCs by PE2 coating. (*A*) Schematic view showing that OC/PE2 system reduces trypsin digestion of fluorescein-labeled BSA encapsulated in the OCs. Adapted with permission from PDB ID: 1S0Q (69). (*B*) Fluorescence kinetics shows enhanced fluorescence of the fluorescein-labeled BSA upon trypsin cleavage (λ_{ex}, 490 nm; λ_{em}, 525 nm, 37 °C).

ability to modulate the desired release during the drug-delivery processes can be useful for controlling its biological effect.

We further demonstrated that surface coating of OCs with **PE2** provides protease resistance to proteins encapsulated in the OC structures. Here, bovine serum albumin (BSA) was modified with fluorescein and encapsulated in the bare OC and OC/PE2 structures via DNA hybridization (*Materials and Methods*). The fluorescence signal was self-quenched due to multiple fluorescein moieties labeled on a single BSA (64). Fluorescence recovery was attained in the presence of trypsin, which catalyzed hydrolysis of BSA preferentially at sites of lysine and arginine (65), and subsequently released the fluorescein-conjugated fragments (schematic in Fig. 7*A*). In the presence of trypsin, an 85% increase in the fluorescence intensity was observed in the fluorescein-labeled BSA in solution (*SI Appendix*, Fig. S27). This fluorescence enhancement representing trypsin digestion of the target BSA sequences was reduced to ~40% by protein encapsulation inside the OCs and further reduced to ~14% by **PE2** coating on the OC surface (*SI Appendix*, Fig. S28). In addition, the fluorescence kinetics assay showed ~3× slower trypsin digestion with **PE2** coating (Fig. 7*B*). Therefore, we believe that peptoid coating can increase protection of biological cargos inside OCs from solution environments. Note

that higher levels of trypsin (0.1 to 5 μM) in the OC solution were examined by TEM imaging, and no observable effect on the OC structures was found (*SI Appendix*, Fig. S29).

Finally, we anticipated that the peptoid-protected OCs could be modified with different biological moieties by incorporating reactive groups into the peptoid sequences. To prove this, two clickable peptoids (brush and block types, **PE8** and **PE9**) were synthesized (schematic in Fig. 8*A*) and used to stabilize OCs. Azide-Fluor 488 (Sigma) was then conjugated to OCs via copper-catalyzed click chemistry. As shown in Fig. 8*C*, the success of surface conjugation was confirmed by the increased fluorescence from OCs. We proposed that the peptoid-protected OCs can also be functionalized with larger biomolecules such as trastuzumab (Tz), an immunoglobulin G1 monoclonal antibody used to treat breast cancers that are human epidermal growth factor receptor 2-positive. To this end, Tz was conjugated with two azide linkers at the C-terminal formylglycine (fGly) residue of the Tz sequence prior to peptoid conjugation (66, 67). This allowed us to perform site-specific antibody–peptoid conjugation via alkyne–azide reaction (*SI Appendix*, Fig. S30), where the active antibody domains were presented in an orientated fashion. As shown in Fig. 8*D*, the conjugation of Tz on OCs was confirmed by immunogold labeling,
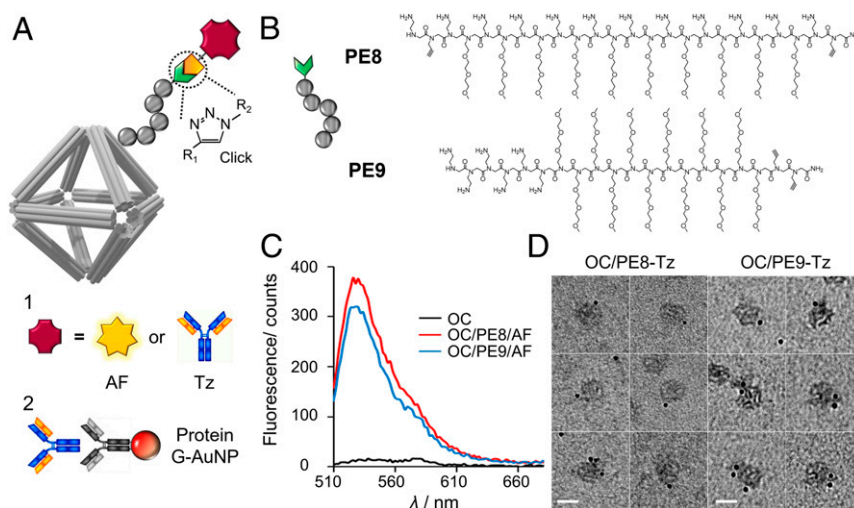

Fig. 8. Surface functionalization of peptoid-stabilized OCs with antibody and fluorophore. (*A*) Schematic view showing alkyne-modified peptoids conjugates azide-modified cargos through click chemistry. **PE8**, Nae–Nprp–(Nae–Nte)$_{10}$–Nae–Nprp; **PE9**, Nae$_6$–Nte$_{12}$–Nprp$_2$, in which prp is the propargyl group. Here, Azide-Fluor 488 (AF) and Tz were used as the presenting cargos (label 1). (*B*) Chemical structure of **PE8** and **PE9**. (*C*) Fluorescence assay of bare OCs, OC/PE8-AF, and OC/PE9-AF extracted from the agarose gel (λ_{ex} = 485 nm and λ_{em} = 510 to 700 nm). (*D*) TEM images show surface coating of OCs with PE8-Tz and PE9-Tz. The samples were labeled with immunogold (label 2 in *A*) prior to TEM imaging. (Scale bars, 50 nm.)

where the Tz was stained by Au NP (6 nm)-modified protein G and visualized by TEM. The Tz-displaying property of OCs can potentially combine with anticancer drugs to provide a combinatory method for cancer therapy.

Conclusion

In this study, we proposed and investigated the use of peptoid architectures to protect DNA origami in different biological environments and for drug delivery, imaging, and cell targeting. Two types ("brush" and "block") of peptoid architectures were studied, where the peptoids comprised positively charged (Nae) moieties and neutral (Nte) moieties. Based on experiments and MD simulations, we showed the sequence dependency of peptoid–DNA interactions, in which brush-type peptoids were advantageous in stabilizing duplex DNA (dsDNA) by multivalent interactions across the DNA backbone. Among the peptoid sequences, the brush-type **PE2** coating on the OCs exhibited the best protection effect toward OC structures, showing enhanced stability when challenged by reduced Mg^{2+} levels or the addition of nuclease. In addition, the peptoid-coated OCs offered a controlled release of Dox and protease resistance for protection of BSA, immobilized inside OCs, from trypsin digestion. Finally, these peptoids were engineered with one or two alkyne groups per chain that enabled the display of a fluorophore and an antibody on OC surfaces through click chemistry. The work presents a systematic study on rationalizing designs of peptoids for enabling a modular strategy of molecular coatings for DNA origamis. The study shows that peptoid-coated DNA origami may serve as a multifunctional fabrication platform for targeted drug delivery, therapeutics, and sensing.

Materials and Methods

Detailed materials, experimental procedures and characterization compounds, including mass spectrometry, AGE, TEM, DLS, SAXS, and fluorescence assays, are available in *SI Appendix*.

Data Availability. All data supporting the findings of this study are available within this article and *SI Appendix* or from the corresponding author on reasonable request.

1. N. C. Seeman, DNA in a material world. *Nature* **421**, 427–431 (2003).
2. C. Lin, Y. Liu, H. Yan, D. N. A. Designer, Designer DNA nanoarchitectures. *Biochemistry* **48**, 1663–1674 (2009).
3. A. V. Pinheiro, D. Han, W. M. Shih, H. Yan, Challenges and opportunities for structural DNA nanotechnology. *Nat. Nanotechnol.* **6**, 763–772 (2011).
4. P. W. K. Rothemund, Folding DNA to create nanoscale shapes and patterns. *Nature* **440**, 297–302 (2006).
5. C. A. Mirkin, R. L. Letsinger, R. C. Mucic, J. J. Storhoff, A DNA-based method for rationally assembling nanoparticles into macroscopic materials. *Nature* **382**, 607–609 (1996).
6. C. M. Niemeyer, W. Bürger, J. Peplies, Covalent DNA-streptavidin conjugates as building blocks for novel biometallic nanostructures. *Angew. Chem. Int. Ed. Engl.* **37**, 2265–2268 (1998).
7. K. Keren et al., Sequence-specific molecular lithography on single DNA molecules. *Science* **297**, 72–75 (2002).
8. W. E. Ford, O. Harnack, A. Yasuda, J. M. Wessels, Platinated DNA as precursors to templated chains of metal nanoparticles. *Adv. Mater.* **13**, 1793–1797 (2001).
9. A. P. Alivisatos et al., Organization of 'nanocrystal molecules' using DNA. *Nature* **382**, 609–611 (1996).
10. D. Nykypanchuk, M. M. Maye, D. van der Lelie, O. Gang, DNA-guided crystallization of colloidal nanoparticles. *Nature* **451**, 549–552 (2008).
11. Y. Zhang, F. Lu, K. G. Yager, D. van der Lelie, O. Gang, A general strategy for the DNA-mediated self-assembly of functional nanoparticles into heterogeneous systems. *Nat. Nanotechnol.* **8**, 865–872 (2013).
12. A. R. Chandrasekaran, O. Levchenko, DNA Nanocages. *Chem. Mater.* **28**, 5569–5581 (2016).
13. A.-K. Schneider, C. M. Niemeyer, DNA surface technology: From gene sensors to integrated systems for life and materials sciences. *Angew. Chem. Int. Ed. Engl.* **57**, 16959–16967 (2018).
14. B. Zhu, L. Wang, J. Li, C. Fan, Precisely tailored DNA nanostructures and their theranostic applications. *Chem. Rec.* **17**, 1213–1230 (2017).
15. Y. Zhang et al., Programmable and multifunctional DNA-based materials for biomedical applications. *Adv. Mater.* **30**, 1703658 (2018).
16. J. Fu, M. Liu, Y. Liu, H. Yan, Spatially-interactive biomolecular networks organized by nucleic acid nanostructures. *Acc. Chem. Res.* **45**, 1215–1226 (2012).
17. J. Li, C. Fan, H. Pei, J. Shi, Q. Huang, Smart drug delivery nanocarriers with self-assembled DNA nanostructures. *Adv. Mater.* **25**, 4386–4396 (2013).
18. Y. Amir et al., Universal computing by DNA origami robots in a living animal. *Nat. Nanotechnol.* **9**, 353–357 (2014).
19. S. M. Douglas, I. Bachelet, G. M. Church, A logic-gated nanorobot for targeted transport of molecular payloads. *Science* **335**, 831–834 (2012).
20. K. E. Bujold, J. C. C. Hsu, H. F. Sleiman, D. N. A. Optimized, Optimized DNA "nanosuitcases" for encapsulation and conditional release of siRNA. *J. Am. Chem. Soc.* **138**, 14030–14038 (2016).
21. V. J. Schüller et al., Cellular immunostimulation by CpG-sequence-coated DNA origami structures. *ACS Nano* **5**, 9696–9702 (2011).
22. G. Grossi, M. Dalgaard Ebbesen Jepsen, J. Kjems, E. S. Andersen, Control of enzyme reactions by a reconfigurable DNA nanovault. *Nat. Commun.* **8**, 992 (2017).
23. A. Ora et al., Cellular delivery of enzyme-loaded DNA origami. *Chem. Commun. (Camb.)* **52**, 14161–14164 (2016).
24. Q. Jiang et al., DNA origami as a carrier for circumvention of drug resistance. *J. Am. Chem. Soc.* **134**, 13396–13403 (2012).
25. Q. Zhang et al., DNA origami as an in vivo drug delivery vehicle for cancer therapy. *ACS Nano* **8**, 6633–6643 (2014).
26. W. Sun et al., Cocoon-like self-degradable DNA nanoclew for anticancer drug delivery. *J. Am. Chem. Soc.* **136**, 14722–14725 (2014).
27. S. M. Douglas et al., Self-assembly of DNA into nanoscale three-dimensional shapes. *Nature* **459**, 414–418 (2009).
28. J. Hahn, S. F. J. Wickham, W. M. Shih, S. D. Perrault, Addressing the instability of DNA nanostructures in tissue culture. *ACS Nano* **8**, 8765–8775 (2014).
29. C. Kielar et al., On the stability of DNA origami nanostructures in low-magnesium buffers. *Angew. Chem. Int. Ed. Engl.* **57**, 9470–9474 (2018).
30. H. Kim, S. P. Surwade, A. Powell, C. O'Donnell, H. Liu, Stability of DNA origami nanostructure under diverse chemical environments. *Chem. Mater.* **26**, 5265–5273 (2014).
31. E. Benson et al., DNA rendering of polyhedral meshes at the nanoscale. *Nature* **523**, 441–444 (2015).
32. E. Benson et al., Effects of design choices on the stiffness of wireframe DNA origami structures. *ACS Nano* **12**, 9291–9299 (2018).
33. R. Veneziano et al., Designer nanoscale DNA assemblies programmed from the top down. *Science* **352**, 1534 (2016).
34. H. Jun et al., Automated sequence design of 3D polyhedral wireframe DNA origami with honeycomb edges. *ACS Nano* **13**, 2083–2093 (2019).
35. T. Gerling, M. Kube, B. Kick, H. Dietz, Sequence-programmable covalent bonding of designed DNA assemblies. *Sci. Adv.* **4**, eaau1157 (2018).
36. V. Cassinelli et al., One-step formation of "chain-armor"-stabilized DNA nanostructures. *Angew. Chem. Int. Ed. Engl.* **54**, 7795–7798 (2015).
37. N. Ponnuswamy et al., Oligolysine-based coating protects DNA nanostructures from low-salt denaturation and nuclease degradation. *Nat. Commun.* **8**, 15654 (2017).
38. J. K. Kiviaho et al., Cationic polymers for DNA origami coating—examining their binding efficiency and tuning the enzymatic reaction rates. *Nanoscale* **8**, 11674–11680 (2016).
39. N. P. Agarwal, M. Matthies, F. N. Gür, K. Osada, T. L. Schmidt, Block copolymer micellization as a protection strategy for DNA origami. *Angew. Chem. Int. Ed. Engl.* **56**, 5460–5464 (2017).
40. J. Mikkilä et al., Virus-encapsulated DNA origami nanostructures for cellular delivery. *Nano Lett.* **14**, 2196–2200 (2014).
41. H. Auvinen et al., Protein coating of DNA nanostructures for enhanced stability and immunocompatibility. *Adv. Healthc. Mater.* **6**, 1700692 (2017).
42. J. Sun, R. N. Zuckermann, Peptoid polymers: A highly designable bioinspired material. *ACS Nano* **7**, 4715–4732 (2013).
43. G. M. Figliozzi, R. Goldsmith, S. C. Ng, S. C. Banville, R. N. Zuckermann, Synthesis of N-substituted glycine peptoid libraries. *Methods Enzymol.* **267**, 437–447 (1996).

CHEMISTRY

APPLIED BIOLOGICAL SCIENCES

44. A. M. Webster, S. L. Cobb, Recent advances in the synthesis of peptoid macrocycles. *Chemistry* **24**, 7560–7573 (2018).

45. S. Xuan *et al.*, Atomic-level engineering and imaging of polypeptoid crystal lattices. *Proc. Natl. Acad. Sci. U.S.A.* **116**, 22491–22499 (2019).

46. S. M. Miller *et al.*, Proteolytic studies of homologous peptide and N-substituted glycine peptoid oligomers. *Bioorg. Med. Chem. Lett* **4**, 2657–2662 (1994).

47. P. A. Wender *et al.*, The design, synthesis, and evaluation of molecules that enable or enhance cellular uptake: Peptoid molecular transporters. *Proc. Natl. Acad. Sci. U.S.A.* **97**, 13003–13008 (2000).

48. J. B. Rothbard *et al.*, Arginine-rich molecular transporters for drug delivery: Role of backbone spacing in cellular uptake. *J. Med. Chem.* **45**, 3612–3618 (2002).

49. T. Schröder *et al.*, Peptoidic amino- and guanidinium-carrier systems: Targeted drug delivery into the cell cytosol or the nucleus. *J. Med. Chem.* **51**, 376–379 (2008).

50. J. E. Murphy *et al.*, A combinatorial approach to the discovery of efficient cationic peptoid reagents for gene delivery. *Proc. Natl. Acad. Sci. U.S.A.* **95**, 1517–1522 (1998).

51. Y. Tian *et al.*, Prescribed nanoparticle cluster architectures and low-dimensional arrays built using octahedral DNA origami frames. *Nat. Nanotechnol.* **10**, 637–644 (2015).

52. Y. Tian *et al.*, Lattice engineering through nanoparticle-DNA frameworks. *Nat. Mater.* **15**, 654–661 (2016).

53. A. R. Statz, R. J. Meagher, A. E. Barron, P. B. Messersmith, New peptidomimetic polymers for antifouling surfaces. *J. Am. Chem. Soc.* **127**, 7972–7973 (2005).

54. S. Xuan *et al.*, Synthesis and characterization of well-defined PEGylated polypeptoids as protein-resistant polymers. *Biomacromolecules* **18**, 951–964 (2017).

55. A. I. Dragan *et al.*, SYBR green I: Fluorescence properties and interaction with DNA. *J. Fluoresc.* **22**, 1189–1199 (2012).

56. H. Zipper, H. Brunner, J. Bernhagen, F. Vitzthum, Investigations on DNA intercalation and surface binding by SYBR Green I, its structure determination and methodological implications. *Nucleic Acids Res.* **32**, e103 (2004).

57. G. Krishnamoorthy, G. Duportail, Y. Mély, Structure and dynamics of condensed DNA probed by 1,1′ -(4,4,8,8-tetramethyl-4,8-diazaundecamethylene)bis[4-[[3- methylbenz-1,3-oxazol-2-yl]methylidine]-1,4-dihydroquinolinium] tetraiodide fluorescence. *Biochemistry* **41**, 15277–15287 (2002).

58. F. Guarnieri, M. Mezei, Simulated annealing of chemical potential: A general procedure for locating bound waters. Application to the study of the differential hydration propensities of the major and minor grooves of DNA. *J. Am. Chem. Soc.* **118**, 8493–8494 (1996).

59. C. H. Spink, J. B. Chaires, Effects of hydration, ion release, and excluded volume on the melting of triplex and duplex DNA. *Biochemistry* **38**, 496–508 (1999).

60. H. Tateishi-Karimta, N. Sugimoto, Control of stability and structure of nucleic acids using cosolutes. *Methods* **67**, 151–158 (2014).

61. D. Miyoshi, H. Karimata, N. Sugimoto, Hydration regulates thermodynamics of G-quadruplex formation under molecular crowding conditions. *J. Am. Chem. Soc.* **128**, 7957–7963 (2006).

62. J. B. Hopkins, R. E. Gillilan, S. Skou, BioXTAS RAW: Improvements to a free open-source program for small-angle X-ray scattering data reduction and analysis. *J. Appl. Cryst.* **50**, 1545–1553 (2017).

63. W. Yang, Nucleases: Diversity of structure, function and mechanism. *Q. Rev. Biophys.* **44**, 1–93 (2011).

64. C. Munkholm, D. R. Parkinson, D. R. Walt, Intramolecular fluorescence self-quenching of fluoresceinamine. *J. Am. Chem. Soc.* **112**, 2608–2612 (1990).

65. L. Hu *et al.*, Highly sensitive fluorescent detection of trypsin based on BSA-stabilized gold nanoclusters. *Biosens. Bioelectron.* **32**, 297–299 (2012).

66. H. Xiao, E. C. Woods, P. Vukojicic, C. R. Bertozzi, Precision glycocalyx editing as a strategy for cancer immunotherapy. *Proc. Natl. Acad. Sci. U.S.A.* **113**, 10304–10309 (2016).

67. M. A. Gray *et al.*, Targeted desialylation overcomes glyco-immune checkpoints and potentiates the anticancer immune response in vivo. ChemRxiv:8187146.v2 (25 November 2019).

68. A. Lahm, D. Suck, DNase I-induced DNA conformation: 2 Å Structure of a DNase I-octamer complex. *J Mol Biol* **222**, 645–667 (1991).

69. J.A. Chamorro Gavilanes, J.A. Cuesta-Seijo, S. Garcia-Granda, Pancratic bovine Trypsin native and inhibited with Benzamidine from synchotron data. Protein Data Bank. http://dx.doi.org/10.2210/pdb1S0Q/pdb. Accessed 10 March 2019.